Experimental and modeling investigation of the laminar flame speeds for ammonia with various oxygen and diluent mixtures

Alaa Hamadi, Nicolas Obrecht, Cyrille Callu, Alessandro Stagni, Tiziano Faravelli, Andrea Comandini, Nabiha Chaumeix

Proceedings of the Combustion Institute 40 (2024) 105387

Contents lists available at ScienceDirect

Proceedings of the Combustion Institute

journal homepage: www.elsevier.com/locate/proci

Experimental and modeling investigation of the laminar flame speeds for ammonia with various oxygen and diluent mixtures

Alaa Hamadi [a], Nicolas Obrecht [b], Cyrille Callu [b], Alessandro Stagni [c], Tiziano Faravelli [c], Andrea Comandini [a], Nabiha Chaumeix [a,*]

[a] CNRS-INSIS, I.C.A.R.E., 1C, Avenue de la recherche scientifique, cedex 2, 45071, Orléans, France
[b] TotalEnergies, Centre de Recherche Solaize, Chemin du Canal – BP22, Cedex, 69360, Solaize, France
[c] CRECK Modeling Lab, Department of Chemistry, Materials and Chemical Engineering "G. Natta", Politecnico di Milano, P.zza Leonardo da Vinci 32, Milano, 20133, Italy

ARTICLE INFO

Keywords:
Ammonia
Laminar flame speed
Markstein length, Spherical bomb

ABSTRACT

The study utilizes two spherical bombs to explore the Laminar Flame Speed (LFS) and Markstein length of oxygen-enriched ammonia flames and ammonia combined with different oxidizers (N_2 with 21% and 30% O_2 and He with 21% O_2). The experiments cover a range of initial conditions, exploring temperatures from 309 K to 423 K and an equivalence ratio spanning from 0.8 to 1.3, all at an initial pressure of 1 bar. At the same time, three established literature mechanisms (Stagni, Shrestha, and Zhang) are used to simulate the data and perform kinetic analysis. A detailed analysis focuses on how the radius of the domain affects LFS, highlighting the importance of a larger domain, in contrast with findings from previous literature. The findings highlighted that, although LFS increased (as expected) with the increase in the initial temperature, the Markstein length remains largely unaffected in oxygen-enriched ammonia flames. This was also calculated using Bechtold and Matalon's approach, and the results were in a good agreement with the experimental values. The study determines alpha exponents across an equivalence ratio range of 0.8 to 1.3, and also found that the inert gas has varying effects on both LFS and Markstein length. Buoyancy effects were noticeable in the ammonia/air experiments, particularly at lower temperatures, challenging existing literature heavily focused on ammonia blends at temperatures below 400 K, potentially contributing to data discrepancies observed in prior studies.

1. Introduction

Ammonia (NH_3) has garnered significant interest on a global scale as nations strive to fulfill their obligations outlined in seminal accords such as the Paris Agreement [1] and Kyoto Protocol [2], which aim to curb greenhouse gas emissions and limit global temperature rise. Nevertheless, ammonia's slow flame propagation, high ignition energy, and high nitrogen oxides (NO_x) emissions have posed significant hurdles to its feasibility as a viable clean energy source. In response to these challenges, extensive research endeavors have focused on unraveling the intricacies of ammonia combustion. Key areas of investigation include laminar flame speed (LFS), ignition delay time, and speciation, all of which are pivotal in understanding and optimizing the combustion of ammonia.

Among these parameters, LFS assumes a central role not only in improving combustion efficiency but also in validating kinetic models that underpin ammonia combustion processes. However, it is worth noting that existing kinetic models often fall short in predicting ammonia's behavior under different operational conditions [3], underscoring the pressing need for more accurate and comprehensive data. Previous literature has discussed the sources of errors in determining LFS [4,5], setting the stage for a deeper examination of this critical parameter.

To address potential inaccuracies, experiments involving oxygen-enriched ammonia flames have been conducted, effectively mitigating the influence of buoyancy effects and bolstering the reliability of the results. Furthermore, this study aims to shed light on the impact of domain size and geometry on the derivation of LFS, comparing the obtained results with the existing literature [6].

The research will also extend its scope to encompass experiments involving ammonia in both air and inert gasses, such as helium, with the objective of assessing the influence of the surrounding medium on

* Corresponding author.
E-mail address: chaumeix@cnrs-orleans.fr (N. Chaumeix).

https://doi.org/10.1016/j.proci.2024.105387
Received 4 December 2023; Accepted 11 June 2024
Available online 27 June 2024

combustion characteristics. Beyond LFS, this study will delve into the analysis of other dynamic parameters including Markstein length, Zeldovich number, and activation energy. These parameters collectively contribute to the intricate chemistry of ammonia combustion, and their exploration promises to deepen our understanding of ammonia's potential as a sustainable and environmentally friendly energy source.

2. Methods

2.1. Experimental set-up

The LFSs are measured in two stainless steel spherical vessels, one with a volume of 56 L (inner diameter: 47.6 cm) and the other with a volume of 93 L (inner diameter: 56.3 cm). Previous articles contain in-depth descriptions of the two spherical bombs, the coupled visualization technique, and flame speed determination [7,8]. Briefly, both the 56 L and 93 L vessels have optical access through opposite quartz windows, with optical diameters of 97 mm and 200 mm, respectively. The vessels' temperature is maintained uniformly through the use of a circulating thermal heating fluid and insulation with a maximum uncertainty of ±1 K. Two tungsten electrodes spaced 2 mm apart are located along the diameter of each sphere. They are connected to a regulated high voltage discharge device that generates a spark in the middle of the spherical reactor to ignite the fuel–air mixtures. The combustion process is monitored using two distinct diagnostics: the pressure time histories are measured using a piezo-electric pressure transducer (Kistler 601A and 6001 models coupled to a Kistler Type 5011B and 5018 Charge Amplifier, respectively), and the expanding flames are visualized and recorded using a Z-type Schlieren setup coupled with a high-speed camera (Phantom V1610). The two diagnostics are synced by a TTL signal generated by a digital delay/pulse generator (Stanford Research System INC.) at the onset of the spark between the electrodes. This synchronization is required to link the pressure rise to the data obtained by fast imaging. The pressure signal, in particular, is used to ensure that all measurements take place under nearly constant pressure conditions. The pressure profiles exhibit an average increase of 0.6% between the start and end times of the captured images. Figs. S1–S6 show examples of flame images and pressure traces.

The captured images are then processed using the Canny method to determine the flame radius as a function of time, from which the adiabatic unstretched gas speed of the burned gasses relative to the flame, S_b^o, and the burned Markstein length, L_b, are iteratively derived using a MATLAB code by solving the non-linear equation developed by Ronney and Sivashinsky [9] and later modified by Kelley and Law [10]:

$\left(\left(S_b/S_b^0\right)^2\right) * ln\left(\left(S_b/S_b^0\right)^2\right) = -(2L_bk)/(S_b^0)$, where k is the stretch rate. The minimum and maximum radii are chosen to prevent the ignition effect and the hydrodynamic instabilities/radiation effects, respectively. Examples of unstretched spatial laminar burning speed extractions using the non-linear method are shown in Figs. S7 and S8. The unburned gases' unstretched laminar flame speed is calculated from the continuity equation through $S_L^o = \rho_b S_b^o/\rho_u$, where ρ_b and ρ_u are calculated using COSILAB's Equilibrium code [11] as the densities of the burnt and unburned gasses, respectively.

The uncertainties associated with determining the LFS stem from several sources, including initial conditions (pressure, temperature, and mixture composition), measurement of the flame radius (with an estimated uncertainty of ±1 pixel), the selected flame radius domain for extrapolation (further elaborated in the Supplementary Material (SM)), experiment repeatability (see Figs. S12–S13), radiative losses (corrected using Yu et al.'s equation [12]), and variations between different extrapolation methods existing in the literature (as illustrated in Fig. S14). The impact of the extrapolation method on experimental outcomes can also be checked by examining the product of the Markstein number and the Karlovitz number, as proposed by Wu et al. [13] (Fig. S15). Accordingly, a global error in S_L^o can be estimated using the error propagation formula for independent uncertainties. More details about the uncertainty calculation process are reported in [14].

Concerning the gasses used in the experiments, Air-Liquide provides NH_3 (≥99.999%), oxygen (≥99.995%), nitrogen (≥99.8%), dry air (≥ 99,9999%) and helium (≥99.999%). The gases are introduced directly into the vessel using the partial pressure approach, with the chamber evacuated to less than 3 Pa beforehand. To minimize errors in mixture preparation, capacitive manometers (MKS Baratron Types 631B, 631F, and 690A) are employed to monitor pressures, with an accuracy of 0.2%, resulting in a maximum 1% uncertainty in the equivalence ratio (φ). The exact compositions of the experimental mixtures are listed in Table 1.

2.2. Kinetic modeling

In this study, three different mechanisms are used, i.e. those by Stagni et al. [15], Shrestha et al. [16] and Zhang et al. [17]. They were developed independently of each other: Stagni et al. (31 species, 203 reactions) developed their mechanism in the context of an experimental study on NH_3/H_2 oxidation, building on top of a previous experimental and theoretical study on pure NH_3 oxidation [18], and validated their mechanism against NH_3/O_2, $NH_3/O_2/N_2$, $NH_3/NO/O_2/N_2$, $NH_3/H_2/O_2/N_2$, NH_3/Argon (AR), $NH_3/H_2/O_2/N_2$/AR, $NH_3/H_2/O_2$/AR, NH_3/O_2/AR, and N_2H_4/N_2 mixtures. Shrestha et al. (125 species, 1099 reactions) updated their previous framework [6], improved for NH_3/H_2 flames and NH_3 flames enriched by O_2, in order to refine their agreement with extinction strain rates of NH_3/H_2/air non-premixed counter flow flames. Their validation dataset included $NH_3/O_2/N_2$, $NH_3/H_2/O_2/N_2$, $NH_3/O_2/N_2$/Ar, $H_2/NH_3/O_2$/Ar, NH_3/O_2/Ar, NH_3/NO/Ar, H_2/O_2/NO/N_2 mixtures. Finally, Zhang et al. (38 species, 263 reactions) set up a kinetic model for pure NH_3 and NH_3/H_2 mixtures, validated against their own data collected in a Jet-stirred reactor as well as a wider range of literature data concerning pure NH_3, NH_3/H_2, H_2/NO, H_2/N2O, NH_3/NO and NH_3/NO_2.

The assessment of laminar flame speeds employs a one-dimensional, premixed, freely propagating flame model in COSILAB. Computational parameters, including a 10 cm domain and grid refinement settings for GRAD and CURV adjusted to $1e^{-4}$, ensure sufficient grid refinement. The convergence criteria lead to a minimum of 250 final grid points, ensuring computational stability and reliability of the results.

3. Results and discussion

3.1. Effect of flame radius domain

Fig. 1(a) compares the current experimental data (red circles) at 323 K and 1 bar for NH_3-enriched air (30% O_2) with the values reported by Shrestha et al. [6] (blue triangles), with Fig. S16 in the SM showing the results at 373 K. The error bars denote the standard deviation derived from three experiments at the same measurement point. Large discrepancies are visible for $\varphi \leq 1.1$. To understand the cause of these discrepancies, we referred to Shrestha's article, examining the selected radius domain and the size of their experimental set-up, which was notably smaller (4.2 L) compared to the one in this study (56 L). Incorporating their extrapolation domain into a 3D plot revealed a noticeable impact on the calculated LFS within their specified domain,

Table 1
Compositions of the gas mixtures used in this study, along with the corresponding conditions. Initial pressure fixed at 1 bar.

Oxidant (%mol)	φ	T_{ini} (K)	Spherical Vessel (L)
$30O_2$+ $70N_2$	0.8 to 1.3	309, 323, 373, 423	56
		309	93
$20.9O_2$+$79.1N_2$	0.8 to 1.3	309, 400	93
$20.9O_2$+79.1He	0.8 to 1.2	400	93

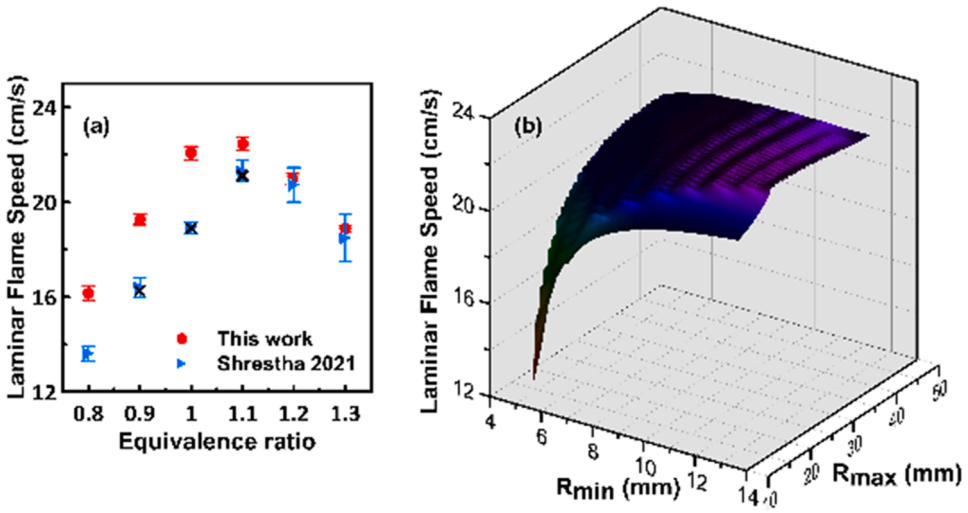

Fig. 1. (a) Laminar flame speed for NH_3 in enriched air at $P_{ini} = 1$ bar and $T_{ini} = 323$ K. Red circles are the present work. The blue triangles are the data from [6]. The cross symbols are the present work measured in the same domain as in [6]. (b) Laminar flame speed as a function of fitting domain for φ=1, including Shrestha's domain.

which then stabilizes beyond that range (Fig. 1(b)). Employing the same extrapolation domain as Shrestha yielded an identical LFS values (as depicted by the cross symbols in Fig. 1(a)).

To further validate the accuracy of the data and demonstrate the independence of the determined LFS from the domain, several experiments are conducted using a larger spherical bomb (93 L) for NH_3-enriched air at 309 K and 1 bar. The results obtained from these experiments were identical to those obtained from the 56 L vessel (Fig. 2).

The 3D plots, as detailed in the SM, effectively mitigate uncertainties arising from the selection of the flame radius domain, offering robust evidence for the accuracy and credibility of the reported LFS values.

3.2. NH_3-enriched air (30% O_2) mixtures

In Fig. 3(a), LFS profiles for $NH_3/O_2/N_2$ with 30% O_2 content are displayed at four distinct temperatures: 309 K, 323 K, 373 K, and 423 K, all at 1 bar, as a function of φ. These profiles include measurements and simulations using three different kinetic models from the literature. The experimental data demonstrates that an increase in temperature leads to an increase in the LFS, and this same trend is corroborated by the predictions of the kinetic models. Moreover, the Zhang mechanism exhibits an under estimation of the experimental LFS data across all temperatures. Conversely, the simulated flame speeds using the Shrestha and Stagni mechanisms demonstrate a satisfactory agreement with the experimental LFS, falling within the bounds of uncertainty error. The correction concerning S_L° for radiative losses, which is considered a part of the uncertainty error, is shown in Fig. S17 for the different temperatures.

Temperature has varying effects on S_L° depending on the equivalence ratio. To assess the impact of initial gas temperature on S_L°, a widely utilized empirical equation is employed: $S_L^\circ(T_i)/\ S_L^\circ(T_0) = (T_i/T_0)^\alpha$. Here the subscript 'i' denotes values at the expected conditions, whereas the subscript '0' refers to reference conditions (309 K and 1 bar in this study). Fig. 3(b) illustrates the α exponent derived from our measurements as a function of φ, as well as the simulations. Uncertainties for power exponent alpha are assessed as described in the work by Alekseev et al. [19]. While all the models are able to depict the trend, the model by Shrestha et al. accurately captures the experimental results within the error bar.

To explore the important reactions influencing $NH_3/O_2/N_2$ LFS, a sensitivity analysis to laminar flame speed is conducted at φ=1, 1 bar and 423 K (Fig. 4; additional temperatures in Figs. S18–S20) across various mechanisms. Remarkably, the sensitive reactions remained consistent despite temperature variations. Positive sensitivity denotes promoting effect on reactivity (increased flame speed), while negative sensitivity indicates an inhibiting one. The pivotal chain branching

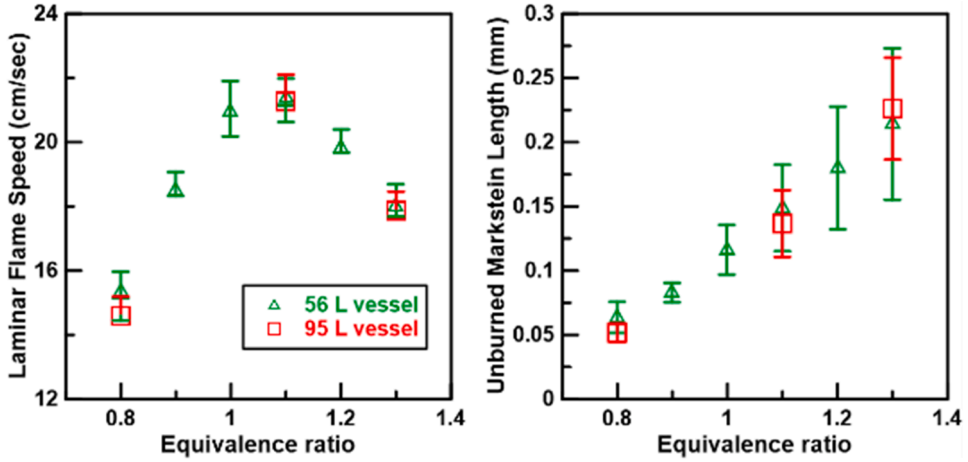

Fig. 2. Comparing Laminar Flame Speed and Markstein Length of NH_3 in enriched air at $P_{ini} = 1$ bar and $T_{ini} = 309$ K using spherical bombs of two different volumes.

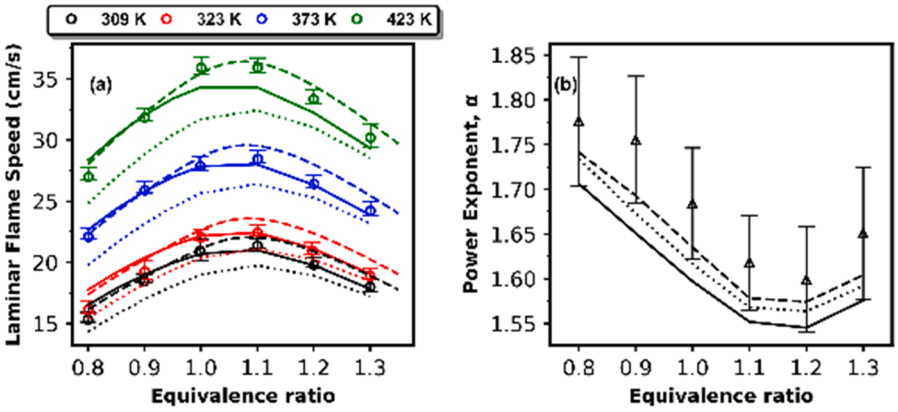

Fig. 3. (a) LFS of oxygen-enriched ammonia flames (30% O_2) versus φ for four different temperatures at P_{ini} = 1 bar. (b) Power exponent, α, versus φ. Symbols: experiments; Solid lines: simulations using Stagni et al. model [15]; Dashed lines: simulations using the Shrestha et al. 2022 model [16]; Dotted lines: simulations using the Zhang et al. 2021 model [17].

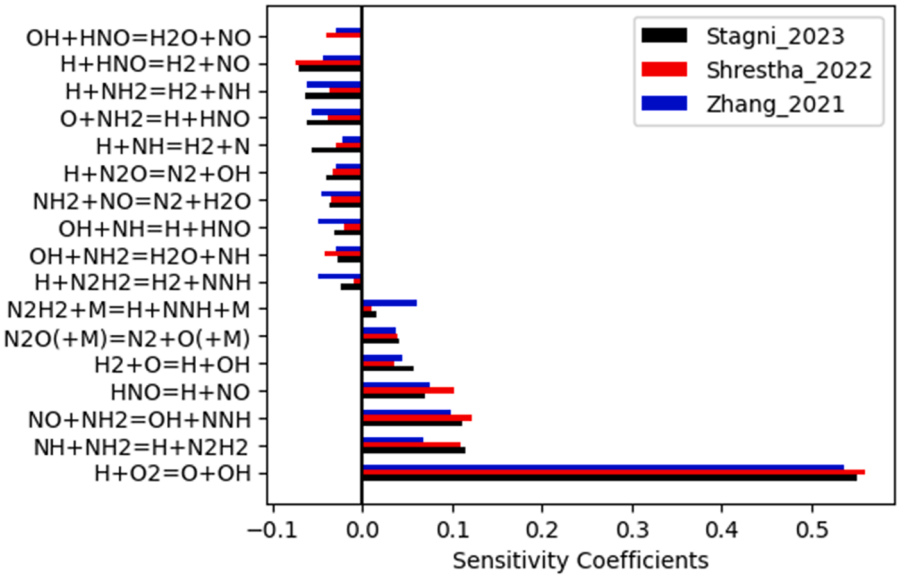

Fig. 4. Reaction sensitivity analysis for LFS of oxygen-enriched ammonia flames (30% O_2) at φ=1, 1 bar and 423 K with different mechanisms.

reaction (H + O_2=OH+O) consistently emerged as the most sensitive across all mechanisms, closely followed by the reaction of NH_2 with NH and NO, leading to the production of highly reactive radicals H and OH. Apart from these reactions, the remaining crucial reactions are consistent across the mechanisms, and there is a notable overlap observed among several reactions shared between Stagni's mechanism and the other two. Consequently, the variation in flame speeds among the different mechanisms is attributed to the value chosen for the different reaction rates, as the pathways are common in all of the three mechanisms.

Fig. 5 shows the Markstein lengths (L_u) versus the equivalence ratio, where $L_u = \rho_b L_b/\rho_u$, at four distinct initial temperatures for oxygen-enriched ammonia flames (30% O_2). The error bars accompanying the experimental values of L_u encompass uncertainties stemming from the measured flame radius (maximum 0.1%), repeatability (Fig. S12), and the extrapolation method (Fig. S21), with the latter exhibiting the highest uncertainty. The positivity of L_u indicates the flame's stability across the entire range of equivalence ratios. Additionally, within the scope of experimental error, no observable temperature dependency is noted. L_u increases monotonically with the increase in the equivalence ratio. Ammonia-air flames show a similar tendency [20,21].

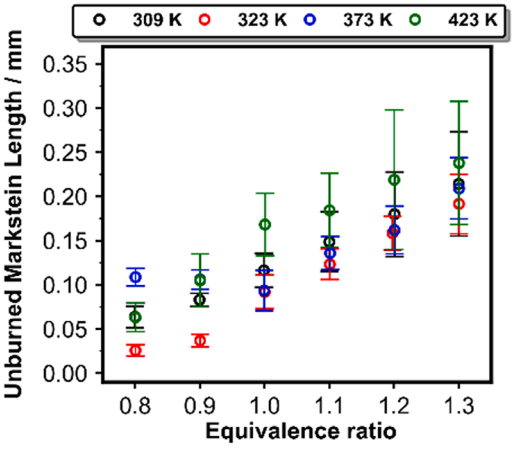

Fig. 5. Effect of the temperature on the unburned Markstein length for oxygen-enriched ammonia flames (30% O_2) versus φ at 1 bar.

Assessing the influence of initial temperature on the Markstein length involves calculating the Markstein number, Ma calc, following Bechtold and Matalon's approach [22]:

$$Ma_{\text{calc}} = L_u/\delta_f = \alpha - ((\sigma - 1)\cdot\gamma_1)/\sigma \quad (1)$$

where $\sigma = \rho_u/\rho_b$, $\alpha = \gamma_1 + 0.5\cdot\beta\cdot(Le_{eff} - 1)\cdot\gamma_2$, $\beta = (E_a\cdot(T_{ad} - T_{ini}))/(R\cdot T_{ad}{}^2)$, $\gamma_1 = (2\cdot\sigma)/(V_\sigma + 1)$, and $\gamma_2 = 4/(\sigma - 1)\{\sqrt{\sigma} - 1 - \ln(0.5\cdot(\sqrt{\sigma} + 1))\}$. It is essential to note that γ_1 and γ_2 are determined based on the thermal conductivity (λ) temperature dependency i.e. $\lambda = f(T)$. Le_{eff}, E_a, T_{ad} and δ_f represent the effective Lewis number, the global activation energy, the adiabatic temperature and the flame thickness respectively.

To estimate Ma_{calc} , initial estimation of several crucial parameters is necessary:

- Flame thickness, $\delta_f = (\lambda/C_p)/(\rho_u \bullet S_L^\circ)$, where the ratio of thermal conductivity to heat capacity (λ/C_p) is evaluated for the unburned gas mixture at the average temperature between the unburned and the adiabatic-flame temperature [23].
- Activation energy, E_a, using thermal explosion theory as thoroughly described in [24].
- Zeldovich number, β, according to [22].
- Effective Lewis number, Le_{eff}, as defined by Addabbo et al. [25].

To compute the different parameters, the thermal and transport data from Stagni et al. [15] and Shrestha et al. [16] are used. The notable resemblance between Figs. 6 and 7 and S22 and S23 signifies significant similarity in both thermodynamics and transport, as elaborated in subsequent paragraphs. The observed deviation in flame speed when using Zhang's mechanism arises from kinetics rather than variations in thermodynamics and transport. Employing their transport and thermodynamic data yield comparable outcomes to the other two mechanisms, although these results aren't reported here.

Fig. 6 illustrates the flame thickness obtained using the Stagni mechanism (Fig. S22 utilizing the Shrestha mechanism) against the equivalence ratio for various initial temperatures at 1 bar for $NH_3/O_2(30\%)/N_2$ mixtures. The flame thickness is the smallest at $\varphi = 1.1$ for all initial mixture temperatures, because the LFS is the fastest at this equivalence ratio. Moreover, as the initial mixture temperature increases, there is a decrease in the preheating zone thickness.

Comparison between the Ma_{calc} and Ma_{exp} is depicted in Figs. 7 and 8 utilizing both Stagni and Shrestha mechanisms. Both the calculated and measured Markstein numbers, *Ma*, exhibit the same trend as a function of equivalence ratio across all the studied temperatures. Notably, the computed Ma_{calc} shows no dependency on the initial temperature,

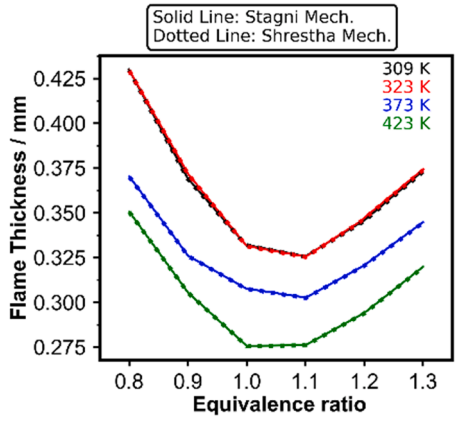

Fig. 6. Effect of the temperature on flame thickness derived using both Stagni and Shrestha mechanisms for oxygen-enriched ammonia flames (30% O_2) versus φ at 1 bar.

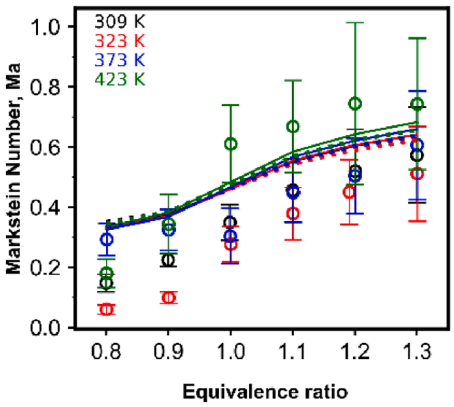

Fig. 7. Effect of the temperature on the calculated, Ma_{calc}, and experimental, Ma_{exp}, Markstein numbers for oxygen-enriched ammonia flames (30% O_2) versus φ at 1 bar. Symbols: experiments; Solid lines: simulations using Stagni et al. model [15]; Dotted lines: simulations using the Shrestha et al. 2022 model [16].

contrary to experimental observations where there's no discernible dependence up to 373 K, while at 423 K, the observed values are higher (Fig. 7). It's evident that *Ma* increases in tandem with the equivalence ratio, akin to the Markstein length's behavior. Despite L_u exhibiting minimal sensitivity to temperature, an impact on *Ma* emerges above 373 K. At 423 K, the effect of temperature on *Ma* becomes apparent, potentially correlated with the remarkably reduced flame thickness observed at this temperature.

As shown in Fig. 8, the calculated Markstein number closely matches the experimental values. It accurately captures the values for equivalence ratios greater than or equal to one across all temperatures within the bounds of uncertainty. Additionally, for the 373 K and 423 K cases, it also captures the values for equivalence ratios below one. This strong agreement between the calculated and experimental Markstein numbers demonstrates the robustness of the detailed kinetic mechanism used in the simulations. The slight deviations at lower temperatures and lean conditions might be due to limitations in the kinetic model or experimental uncertainties.

The primary aim of this study revolves around comparing the measured L_u with its calculated counterpart, derived by multiplying the Markstein number with the flame thickness. In Fig. 9, a comparison between the measured and calculated Markstein lengths using both Stagni and Shrestha models is depicted for various initial temperatures across different equivalence ratios at a pressure of 1 bar. Remarkably, the calculated Markstein lengths closely align with the measured ones, accounting for uncertainty errors, at 373 K and 423 K temperatures. However, at equivalence ratios higher than 1, the calculated length closely corresponds to the measured one for 309 K and 323 K. Furthermore, both the calculated and measured lengths exhibit a similar trend, affirming the reliability of the employed methodology. This robust agreement suggests a comprehensive understanding of the combustion dynamics under different conditions, emphasizing the utility of the proposed approach for predicting Markstein lengths accurately. Such findings not only validate the computational models but also provide insights into the intricate interplay between flame behavior and chemical kinetics, offering potential avenues for further investigation and optimization in combustion systems.

3.3. Role of oxidizer in NH_3 combustion

Fig. 10(a) depicts the LFS versus equivalence ratio for an $NH_3/O_2/He$ blend 21% O_2 at 400 K and 1 bar, alongside with model predictions. The models by Shrestha et al. [16] and Zhang et al. [17] respectively overestimate and underestimate the measured values of LFS across the entire range. Conversely, the model proposed by Stagni et al. [15] anticipates

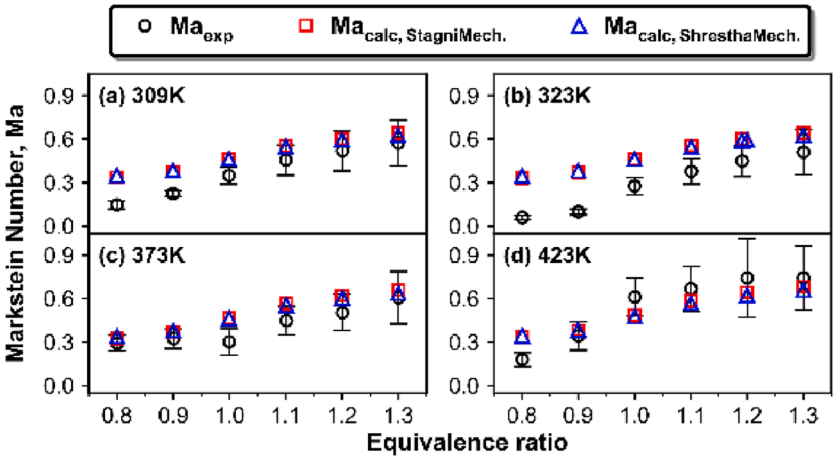

Fig. 8. The calculated, Ma_{calc}, and experimental, Ma_{exp}, Markstein numbers for oxygen-enriched ammonia flames (30% O_2) versus φ at 1 bar and 4 different temperatures.

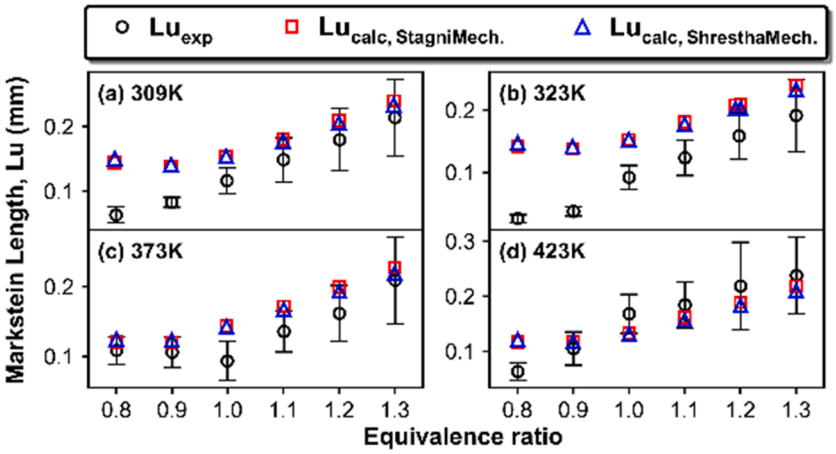

Fig. 9. The calculated and experimental Markstein lengths for oxygen-enriched ammonia flames (30% O_2) versus φ at 1 bar and 4 different temperatures.

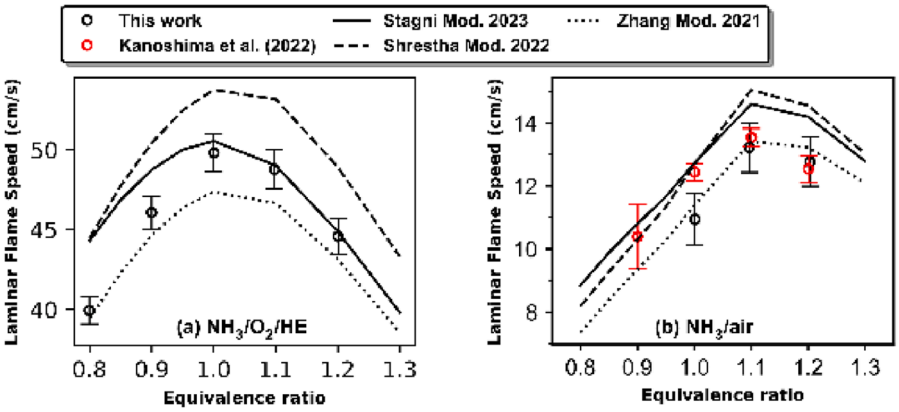

Fig. 10. LFS for (a) NH_3/O_2/He and (b) NH_3/air are plotted as a function of φ at $T = 400$ K and $P = 1$ bar, together with predicted values using three mechanisms; Solid lines: simulations using Stagni et al. model [15]; Dashed lines: simulations using the Shrestha et al. 2022 model [16]; Dotted lines: simulations using the Zhang et al. 2021 model [17]. Red symbols: measurements from [20].

slightly higher laminar flame speeds under lean conditions and demonstrates significantly improved agreement at stoichiometric and rich sides. As stated in the experimental section, the uncertainty in the LFS stems from various sources, with their effects depicted in Figs. S22–S24 (a) in the SM. Among these sources, the most significant contributor to the error is the extrapolation method. This conclusion gains further support from the product of the Markstein number and the Karlovitz number [13], as all experimental conditions lie beyond the predefined lower and upper boundaries (Fig. S25).

The laminar flame speed for ammonia air under identical conditions

as NH_3/O_2/He is presented in Fig. 10(b), accompanied by model predictions and experimental data sourced from literature [20] under matching conditions. It is important to note that error bars in this study are evaluated as previously outlined. However, for the literature data, the error bars represent solely the standard deviation of the conducted experiments. The experimental findings align with the literature data at φ =1.1 and 1.2, but they are lower at φ =1. Concerning the models, both Stagni and Shrestha mechanisms tend to overestimate the experimental results. However, the Zhang et al. model adequately predicts the experimental outcomes within the error margins.

This experimental configuration includes modifying both the heat capacity and collision efficiency of the inert gas present in the oxidizer. The notable increase in laminar flame speed, in contrast to experiments using O_2/N_2 oxidizer blends, is mainly linked to the elevated adiabatic flame temperature (see Fig. S26).

Fig. 11 depicts L_u against the equivalence ratio for NH_3/O_2/He and NH_3/air at a temperature of 400 K and pressure of 1 bar. The error bars accompanying the experimental L_u values encompass uncertainties originating from the measured flame radius (maximum 0.1%), repeatability (refer to Fig. S22), and the extrapolation method (see Fig. S27), with the latter displaying the most significant uncertainty. The positive L_u values indicate the flame's stability across the entire range of equivalence ratios. In NH_3/O_2/He, L_u exhibits a non-monotonic decrease as the equivalence ratio rises, reaching a minimum around φ =1.1, after which it shows a slight increase. As in oxygen-enriched ammonia flames (30% O_2) case, L_u in NH_3/air demonstrates a monotonic increase with the equivalence ratio. Overall, the inert gasses (He in NH_3/O_2/He and N_2 in NH_3/air) seem to exert distinct influences on L_u, shaping the flame characteristics and sensitivity across different equivalence ratios.

Further experiments involving NH_3/air mixtures are carried out at 1 bar and 309 K. These investigations are pivotal in drawing comparisons with prior experiments. Particularly at 309 K, the impact of buoyancy is markedly apparent. This is clearly visible when comparing the centroid velocity to the burning velocity (V_s=dr_f/dt, *where* r_f *is the flame radius and t is the time*), as Fig. 12 illustrates. Not only is the impact of buoyancy clearly seen in velocity differentials, but it is also evident in the observable behavior of the flame. As buoyancy becomes more significant, the flame loses its typical spherical form, undergoing a rapid decrease in its shape ratio. The appearance of two pressure peaks serves to emphasize this change even more (Fig. S28). The lingering effect of buoyancy continued even at a higher temperature of 400 K, albeit less prominently than at 309 K. Interestingly, its effect is stronger for equivalence ratios outside of the 1–1.2 range (Fig. S29).

A substantial part of the current body of literature concentrates on ammonia blend mixtures in air, particularly at temperatures below 400 K. This particular focus could potentially introduce higher uncertainties in determining LFS, consequently contributing to the discrepancies observed among the data present in the literature.

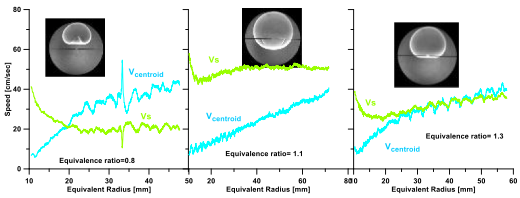

Fig. 12. The centroid velocity and the burning velocity versus radius for NH_3/air at T = 309 K and P = 1 bar at φ=0.8, 1.1 and 1.3.

4. Conclusion

Two distinct spherical bombs are employed to study the LFS and Markstein length in experiments involving oxygen-enriched ammonia mixtures and ammonia paired with varying oxidizers (N_2 and He, both with 21% O_2). The experiments focusing on oxygen-enriched ammonia flames are conducted at initial pressure of 1 bar and initial temperatures of 309, 323, 373 and 423 K over an equivalence ratio range of 0.8–1.3. The findings reveal an increase in LFS with increase in temperature, yet no significant impact is observed on the Markstein length. To simulate the data, three different mechanisms—Stagni, Shrestha, and Zhang—are used. The former two mechanisms demonstrate satisfactory predictive performance when compared with the experimental data. Further examination through sensitivity analysis aimed to identify the most influential reactions affecting the LFS. As expected, the O_2+H=OH+O reaction emerged as the most sensitive among all reactions—a conclusion universally supported in previous literature concerning ammonia combustion. The initial temperature did not manifest any effect on the top ten sensitive reactions influencing the LFS. The theoretical Markstein lengths, computed using the approach of Bechtold and Matalon, based on the Stagni and Shrestha mechanisms, displayed good agreement with the experimental values within the margins of uncertainty errors. The alpha exponent, crucial for calculating flame speeds under specific reference conditions, are determined across an equivalence ratio range of 0.8 to 1.3. Furthermore, a detailed analysis elucidates the impact of domain radius on LFS, juxtaposed with Shrestha's work [6], highlighting the significance of a larger domain.

Additionally, experiments measuring ammonia laminar flame speeds and Markstein length, with helium as an inert gas, are conducted at T = 400 K, P = 1 bar and φ=0.8–1.2. Experiments involving NH_3/air are carried out at an initial pressure of 1 bar, initial temperatures at 309 and 400 K, and φ=0.8–1.3. When comparing the data obtained at 400 K, it was evident that the inert gas had varying effects on both the LFS and Markstein length. In the context of ammonia/air experiments, the impact of buoyancy was observable at both temperatures, albeit more pronounced at 309 K. A substantial portion of the existing literature is heavily centered on ammonia blend mixtures in air, particularly emphasizing temperatures below 400 K. This concentrated focus might

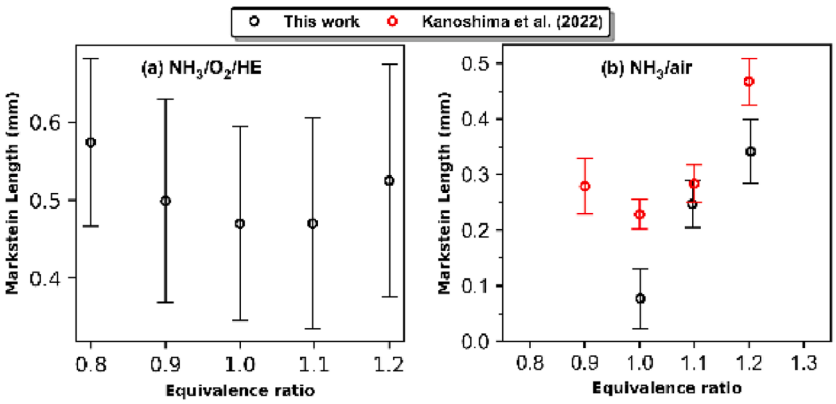

Fig. 11. L_u for (a) NH_3/O_2/He and (b) NH_3/air are plotted as a function of φ at T = 400 K and P = 1 bar. Red symbols: measurements from [20].

introduce increased uncertainties in determining LFS, potentially contributing to the observed discrepancies among the available data in the literature.

Novelty and Significance Statement

The novelty of this research is the measurement of NH3 flames over a large domain of temperature, diluents and equivalence ratios. It is significant because these results point at the origin of the discrepancy in the literature and give a view on how the size of the flame impacts the laminar flame speed. The new data are of great importance for the kinetic validation of NH3 mechanism. For the first time, Markstein lengths have been calculated based on detailed kinetic mechanism adding a parameter to the validation process.

CRediT authorship contribution statement

Alaa Hamadi: performed research, analyzed data, performed the kinetic analyses, wrote the paper **Nicolas Obrecht:** scientific discussion on the research; revised the manuscript **Cyrille Callu:** scientific discussion on the research; revised the manuscript **Alessandro Stagni:** performed flame speed simulation; provided kinetic expertise; revised the manuscript **Tiziano Faravelli:** provided kinetic expertise; revised the manuscript **Andrea Comandini:** designed research, analyzed data; revised the manuscript **Nabiha Chaumeix:** designed research, analyzed data; revised the manuscript.

Declaration of competing interest

The authors declare that they have no known competing financial interests or personal relationships that could have appeared to influence the work reported in this paper.

Acknowledgements

The authors acknowledge the financial support of TotalEnergies One Tech, contract # CT000329- CNRS-249-002.

Supplementary materials

Supplementary material associated with this article can be found, in the online version, at doi:10.1016/j.proci.2024.105387.

References

[1] C.A. Horowitz, Paris agreement, Int. Leg. Mater. 55 (2016) 740–755.
[2] A. Cirman, P. Domadenik, M. Koman, T. Redek, A. Cvetkovska, I. Hribar, R. Intriago, Š. Jurman, A. Korošec, M. Malovrh, B. Milanović, J. Ogrin, A. Paff, M. Poljanc, J. Popović, L. Prošev, N. Seshadri, A. Tomašek, K. Zhang, The Kyoto protocol in a global perspective, Econ. Bus. Rev. 11 (2009) 29–54.
[3] A. Alnasif, S. Mashruk, H. Shi, M. Alnajideen, P. Wang, D. Pugh, A. Valera-Medina, Evolution of ammonia reaction mechanisms and modeling parameters: A review, Appl. Energy Combust. Sci. 15 (2023) 100175.
[4] Z. Chen, On the accuracy of laminar flame speeds measured from outwardly propagating spherical flames: methane/air at normal temperature and pressure, Combust. Flame 162 (2015) 2442–2453.
[5] W. Han, P. Dai, X. Gou, Z. Chen, A review of laminar flame speeds of hydrogen and syngas measured from propagating spherical flames, Appl. Energy Combust. Sci. 1–4 (2020) 100008.
[6] K.P. Shrestha, C. Lhuillier, A.A. Barbosa, P. Brequigny, F. Contino, C. Mounaïm-Rousselle, L. Seidel, F. Mauss, An experimental and modeling study of ammonia with enriched oxygen content and ammonia/hydrogen laminar flame speed at elevated pressure and temperature, Proc. Combust. Inst. 38 (2021) 2163–2174.
[7] A. Comandini, G. Pengloan, S. Abid, N. Chaumeix, Experimental and modeling study of styrene oxidation in spherical reactor and shock tube, Combust. Flame 173 (2016) 425–440.
[8] J. Goulier, N. Chaumeix, F. Halter, N. Meynet, A. Bentaïb, Experimental study of laminar and turbulent flame speed of a spherical flame in a fan-stirred closed vessel for hydrogen safety application, Nucl. Eng. Des. 312 (2017) 214–227.
[9] P.D. Ronney, G.I. Sivashinsky, A theoretical study of propagation and extinction of nonsteady spherical flame fronts, SIAM J. Appl. Math. 49 (1989) 1029–1046.
[10] A.P. Kelley, C.K. Law, Nonlinear effects in the extraction of laminar flame speeds from expanding spherical flames, Combust. Flame 156 (2009) 1844–1851.
[11] COSILAB, The Combustion Simulation Laboratory, Rotexo GmbH & Co., KG, Haan, Germany, 2009. Version 3.3.2, (n.d.
[12] H. Yu, W. Han, J. Santner, X. Gou, C.H. Sohn, Y. Ju, Z. Chen, Radiation-induced uncertainty in laminar flame speed measured from propagating spherical flames, Combust. Flame 161 (2014) 2815–2824.
[13] F. Wu, W. Liang, Z. Chen, Y. Ju, C.K. Law, Uncertainty in stretch extrapolation of laminar flame speed from expanding spherical flames, Proc. Combust. Inst. 35 (2015) 663–670.
[14] D. Nativel, M. Pelucchi, A. Frassoldati, A. Comandini, A. Cuoci, E. Ranzi, N. Chaumeix, T. Faravelli, Laminar flame speeds of pentanol isomers: An experimental and modeling study, Combust. Flame 166 (2016) 1–18.
[15] A. Stagni, S. Arunthanayothin, M. Dehue, O. Herbinet, F. Battin-Leclerc, P. Bréquigny, C. Mounaïm-Rousselle, T. Faravelli, Low- and intermediate-temperature ammonia/hydrogen oxidation in a flow reactor: Experiments and a wide-range kinetic modeling, Chem. Eng. J. 471 (2023) 144577.
[16] D.E. Thomas, K.P. Shrestha, F. Mauss, W.F. Northrop, Extinction and NO formation of ammonia-hydrogen and air non-premixed counterflow flames, Proc. Combust. Inst. 39 (2023) 1803–1812.
[17] X. Zhang, S.P. Moosakutty, R.P. Rajan, M. Younes, S.M. Sarathy, Combustion chemistry of ammonia/hydrogen mixtures: Jet-stirred reactor measurements and comprehensive kinetic modeling, Combust. Flame 234 (2021) 111653.
[18] A. Stagni, C. Cavallotti, S. Arunthanayothin, Y. Song, O. Herbinet, F. Battin-Leclerc, T. Faravelli, An experimental, theoretical and kinetic-modeling study of the gas-phase oxidation of ammonia, React. Chem. Eng. 5 (2020) 696–711.
[19] V.A. Alekseev, M. Christensen, A.A. Konnov, The effect of temperature on the adiabatic burning velocities of diluted hydrogen flames: A kinetic study using an updated mechanism, Combust. Flame 162 (2015) 1884–1898.
[20] R. Kanoshima, A. Hayakawa, T. Kudo, E.C. Okafor, S. Colson, A. Ichikawa, T. Kudo, H. Kobayashi, Effects of initial mixture temperature and pressure on laminar burning velocity and Markstein length of ammonia/air premixed laminar flames, Fuel 310 (2022) 122149.
[21] A. Hayakawa, T. Goto, R. Mimoto, Y. Arakawa, T. Kudo, H. Kobayashi, Laminar burning velocity and Markstein length of ammonia/air premixed flames at various pressures, Fuel 159 (2015) 98–106.
[22] J.K. Bechtold, M. Matalon, The dependence of the Markstein length on stoichiometry, Combust. Flame 127 (2001) 1906–1913.
[23] M. Matalon, Flame dynamics, Proc. Combust. Inst. 32 (2009) 57–82.
[24] Sally Page Moffett Bane, Spark Ignition: Experimental and Numerical Investigation With Application to Aviation Safety, California Institute of Technology, 2010.
[25] R. Addabbo, J.K. Bechtold, M. Matalon, Wrinkling of spherically expanding flames, Proc. Combust. Inst. 29 (2002) 1527–1535.